Supplementary material for: The Matsuno-Gill model on the sphere

Ofer Shamir[1], Chaim I. Garfinkel[2], Edwin P. Gerber[1] and Nathan Paldor[2]†

[1]Courant Institute of Mathematical Sciences, New York University, New York, New York

[2]Fredy and Nadine Herrmann Institute of Earth Sciences, Hebrew University of Jerusalem, Edmond J. Safra Campus, Givat Ram, Jerusalem, 91904, Israel

(Received xx; revised xx; accepted xx)

This supplementary provides additional figures showing the solutions in response to wavenumbers 2 and 8 forcing; the special case of a wavenumber 1 forcing and analysis of this special case; some asymptotic solutions for $\gamma \gg 1$, $\gamma \ll 1$, and $\epsilon^{1/2} \ll 1$; and the wave spectrum for small wavenumber forcing.

Contents

1. Additional solutions for wavenumbers 2 and 8 1
2. The special case of a wavenumber 1 forcing 6
3. Asymptotic forms of the solutions in the vicinity of the poles 9
4. Asymptotic solutions 11
4.1. Asymptotic forms of the solutions for $\gamma \gg 1$ 11
4.2. Asymptotic forms of the solutions for $\gamma \ll 1$ 12
4.3. Asymptotic forms of the solutions for $\epsilon^{1/2} \ll 1$ 15
5. Wave spectrum for small wavenumber forcing 18
6. Sensitivity of the Fourier decomposition to the truncation order 20
7. Flora 21

1. Additional solutions for wavenumbers 2 and 8

In the main text, we have chosen wavenumber $m = 5$ as a representative case due to its correspondence with Matsuno's planner wavenumber $k = 0.5$ at $\epsilon^{1/4} = 10$. Figures 1, 2, 3, and 4, below, show the responses to a Kelvin wave-2, an MRG wave-2, a Kelvin wave-8, and an MRG wave-8, respectively. The observations made in section 4 of the main text for the representative wave-5 forcing are all relevant in these cases as well.

† Email address for correspondence: nathan.paldor@mail.huji.ac.il

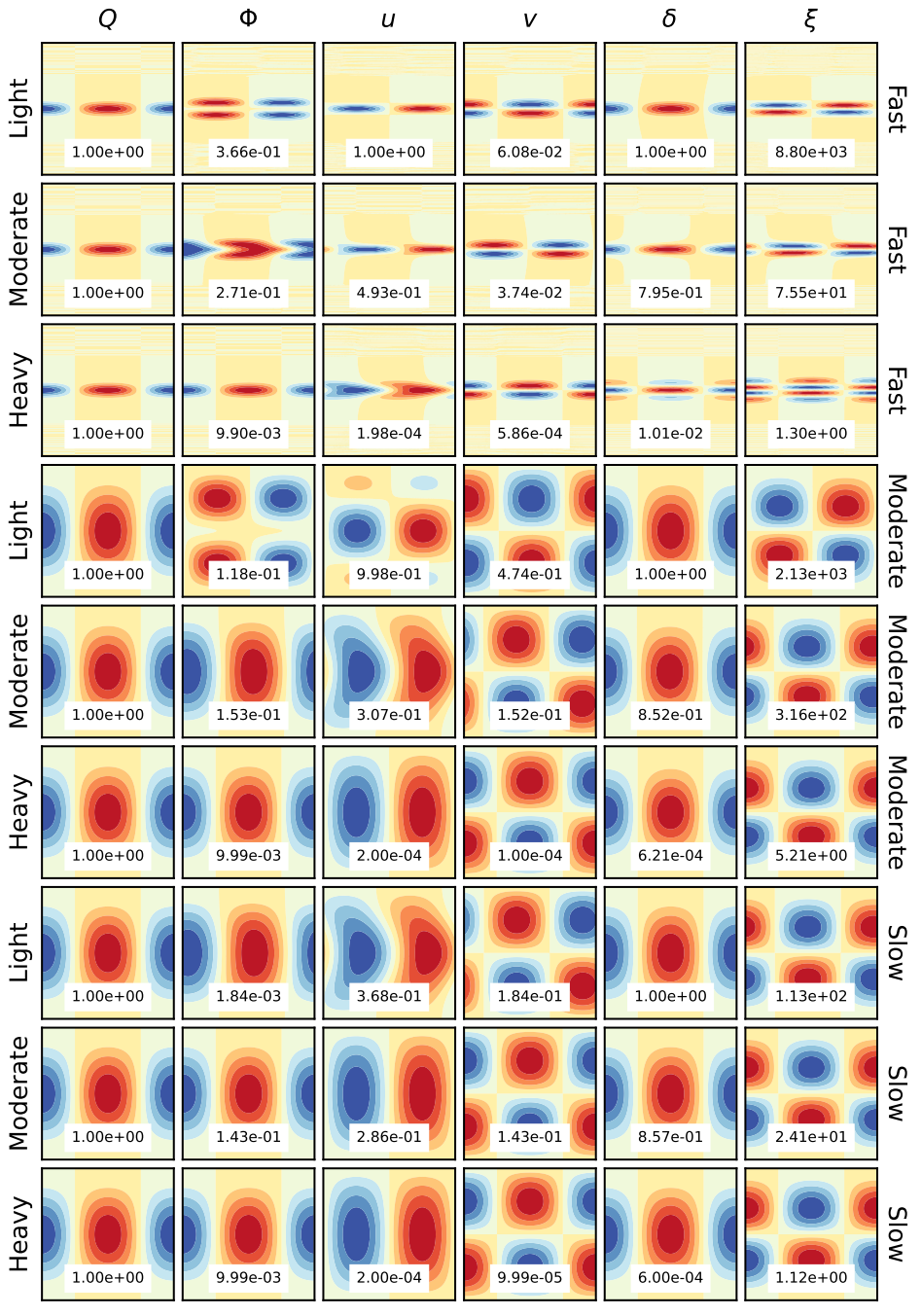


FIGURE 1. Steady response to a symmetric **Kelvin wave-2** forcing. From left to right: the forcing, geopotential height, zonal wind, meridional wind, divergence, and vorticity. The rows correspond to the different samples of the $(\gamma, \epsilon^{1/2})$ plane summarized in table 1 of the main text. The damping and rotation rates for each case (row) are labeled on the left and right edges, respectively. The meridional domain in each panel extends from pole to pole. The longitudinal domain corresponds to 1 zonal period. Contours range from -1 (deep blue) to 1 (strong red) every 0.25. Each panel is normalized on its global absolute maximum, given in white text boxes.

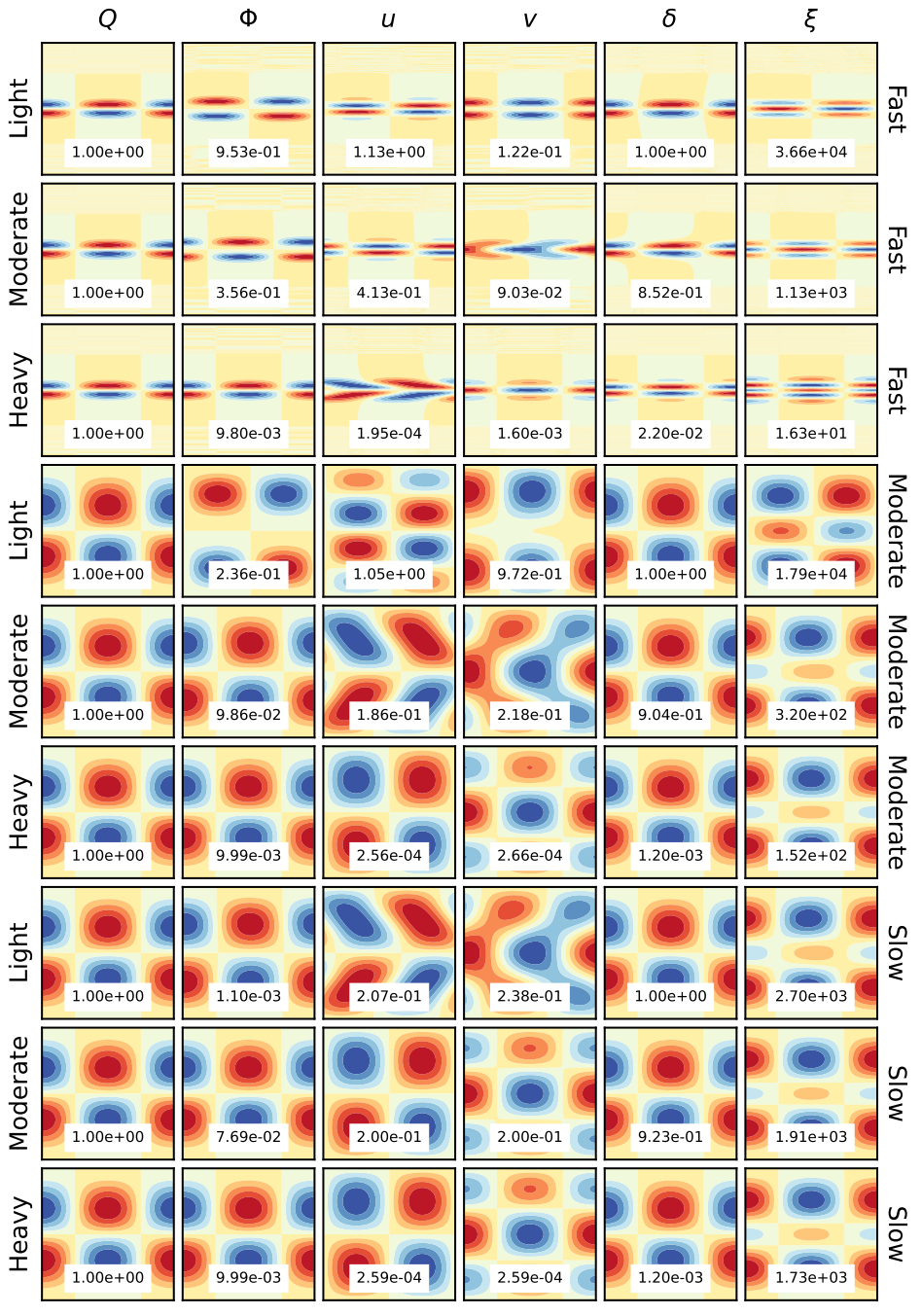


FIGURE 2. Steady response to a symmetric **MRG wave-2** forcing. From left to right: the forcing, geopotential height, zonal wind, meridional wind, divergence, and vorticity. The rows correspond to the different samples of the $(\gamma, \epsilon^{1/2})$ plane summarized in table 1 of the main text. The damping and rotation rates for each case (row) are labeled on the left and right edges, respectively. The meridional domain in each panel extends from pole to pole. The longitudinal domain corresponds to 1 zonal period. Contours range from -1 (deep blue) to 1 (strong red) every 0.25. Each panel is normalized on its global absolute maximum, given in white text boxes.

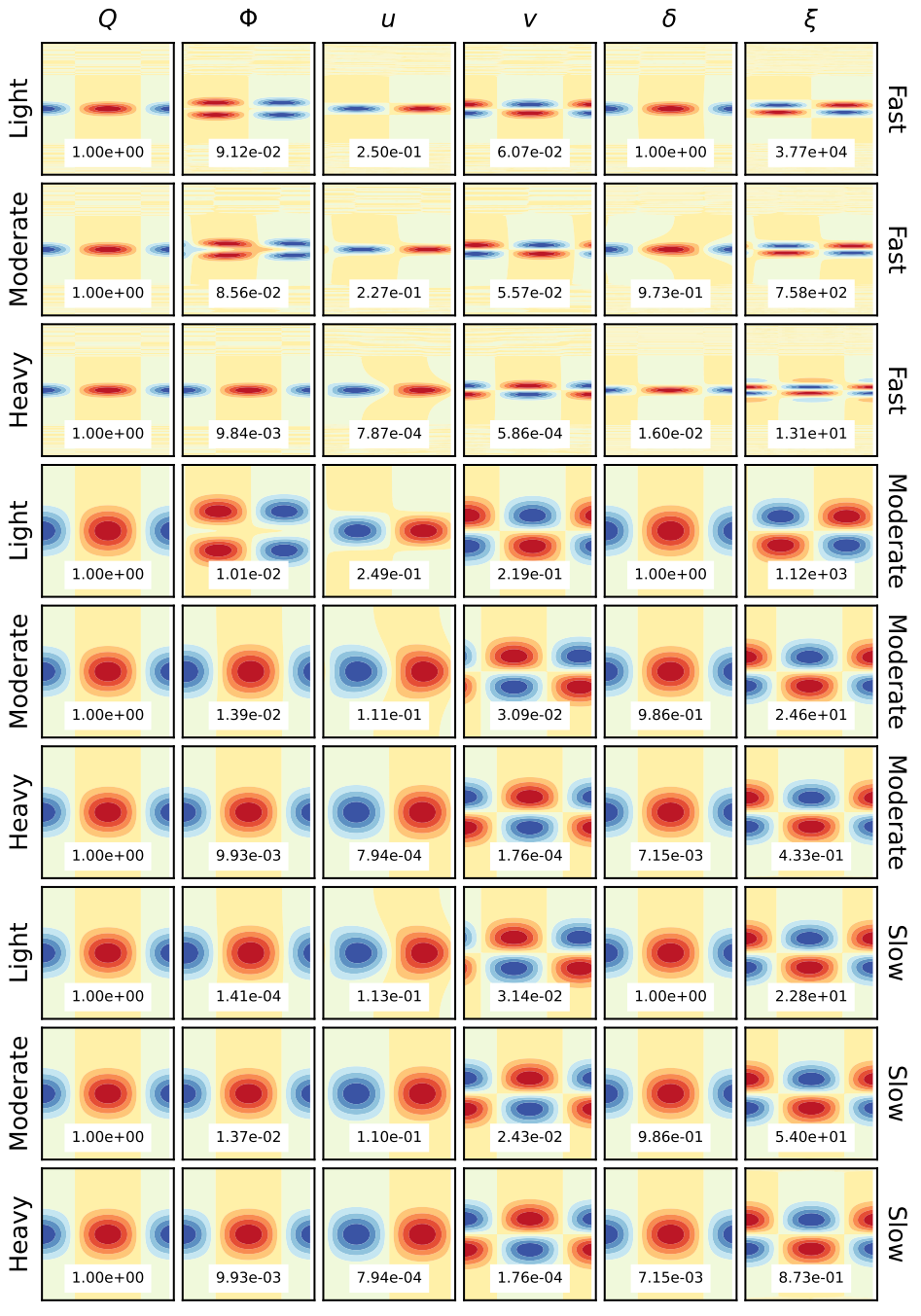


FIGURE 3. Steady response to a symmetric **Kelvin wave-8** forcing. From left to right: the forcing, geopotential height, zonal wind, meridional wind, divergence, and vorticity. The rows correspond to the different samples of the $(\gamma, \epsilon^{1/2})$ plane summarized in table 1 of the main text. The damping and rotation rates for each case (row) are labeled on the left and right edges, respectively. The meridional domain in each panel extends from pole to pole. The longitudinal domain corresponds to 1 zonal period. Contours range from -1 (deep blue) to 1 (strong red) every 0.25. Each panel is normalized on its global absolute maximum, given in white text boxes.

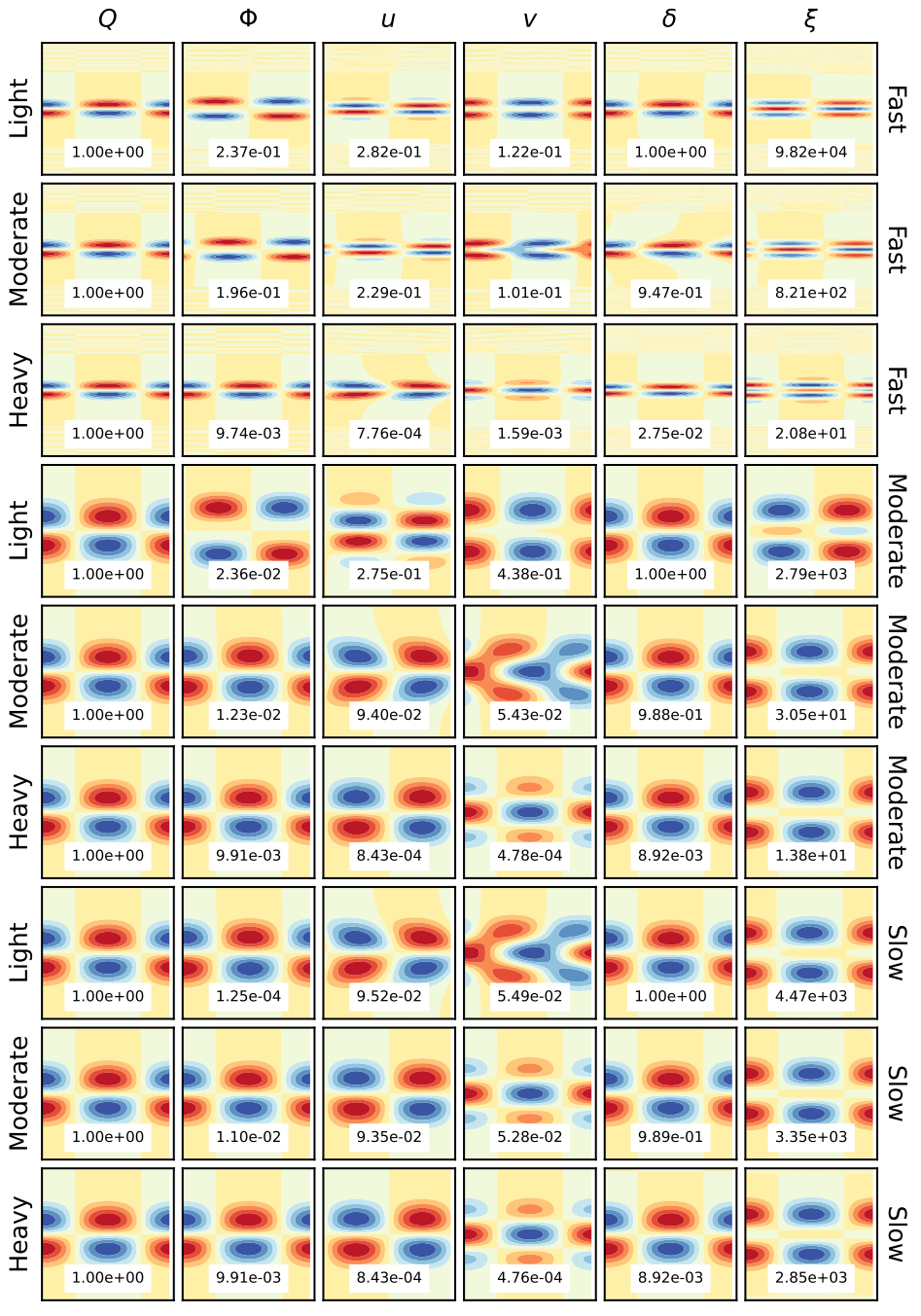


FIGURE 4. Steady response to a symmetric **MRG wave-8** forcing. From left to right: the forcing, geopotential height, zonal wind, meridional wind, divergence, and vorticity. The rows correspond to the different samples of the $(\gamma, \epsilon^{1/2})$ plane summarized in table 1 of the main text. The damping and rotation rates for each case (row) are labeled on the left and right edges, respectively. The meridional domain in each panel extends from pole to pole. The longitudinal domain corresponds to 1 zonal period. Contours range from -1 (deep blue) to 1 (strong red) every 0.25. Each panel is normalized on its global absolute maximum, given in white text boxes.

2. The special case of a wavenumber 1 forcing

The response to a wavenumber 1 forcing is qualitatively different from all other wavenumbers $m > 1$ in that the regular solutions of the Matsuno-Gill model have non-vanishing velocities in the vicinity of the poles. Thus, we now describe the solutions in this special case. Its importance stems from the fact that most large-scale forcing on Earth are expected to have a substantial wave-1 contribution.

Figures 5 and 6 provide the solutions of the Matsuno-Gill model on the sphere in response to a (symmetric) Kelvin wave and an (anti-symmetric) MRG wave, respectively, in the special case of wavenumber 1 forcing. The observations made in section 4 of the main text for the representative wavenumber 5 forcing are all relevant in this case as well. The main difference concerns the behavior of the global solutions-regime. Specifically, the wave-1 response has non-vanishing velocities in the vicinity of the poles, though the forcing vanishes there. This apparent contradiction is alleviated by observing that the divergence does vanish, such that there are no net mass fluxes near the poles. In other words, a wave-1 forcing introduces no superfluous upwelling/downwelling at the poles despite the non-vanishing winds there. These observations are substantiated in section 3. In fact, the non-vanishing velocities are a feature of the free wave modes of the RSWEs. Having said that, a more physically reasonable condition may be that the winds vanish as well.

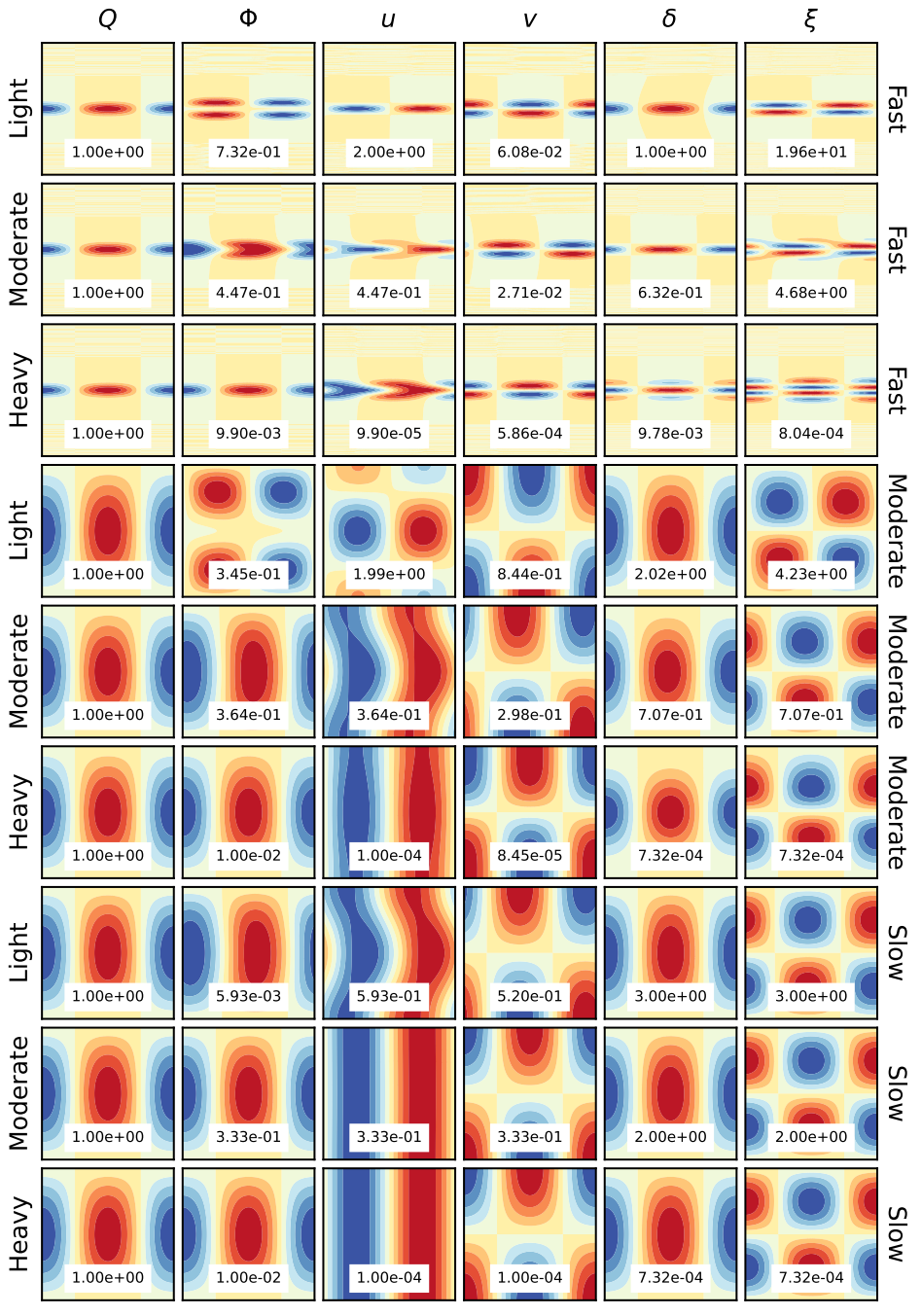


FIGURE 5. Steady response to a symmetric **Kelvin wave-1** forcing. From left to right: the forcing, geopotential height, zonal wind, meridional wind, divergence, and vorticity. The rows correspond to the different samples of the $(\gamma, \epsilon^{1/2})$ plane summarized in table 1 of the main text. The damping and rotation rates for each case (row) are labeled on the left and right edges, respectively. The meridional domain in each panel extends from pole to pole. The longitudinal domain corresponds to 1 zonal period. Contours range from -1 (deep blue) to 1 (strong red) every 0.25. Each panel is normalized on its global absolute maximum, given in white text boxes.

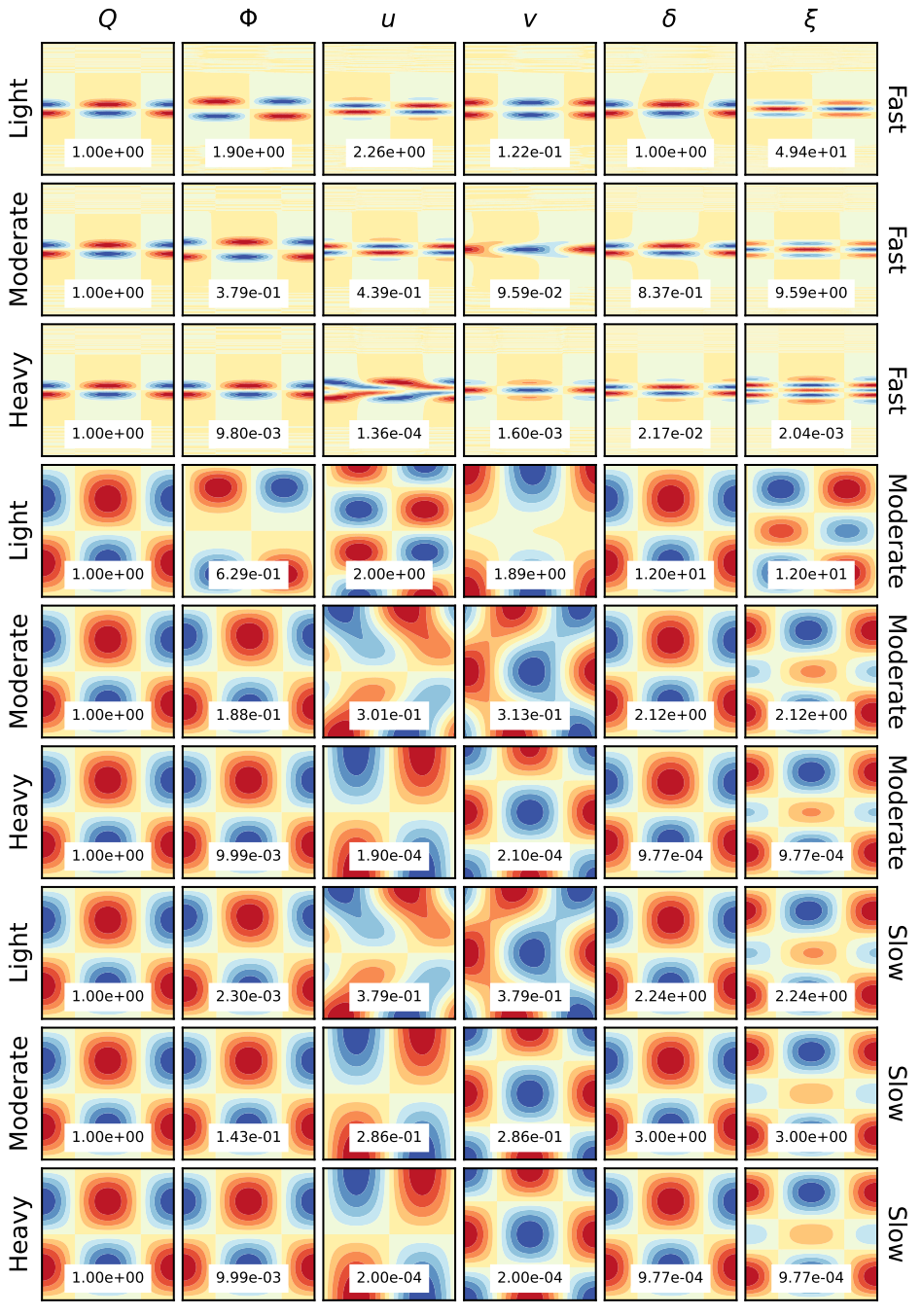


FIGURE 6. Steady response to a symmetric **MRG wave-1** forcing. From left to right: the forcing, geopotential height, zonal wind, meridional wind, divergence, and vorticity. The rows correspond to the different samples of the $(\gamma, \epsilon^{1/2})$ plane summarized in table 1 of the main text. The damping and rotation rates for each case (row) are labeled on the left and right edges, respectively. The meridional domain in each panel extends from pole to pole. The longitudinal domain corresponds to 1 zonal period. Contours range from -1 (deep blue) to 1 (strong red) every 0.25. Each panel is normalized on its global absolute maximum, given in white text boxes.

3. Asymptotic forms of the solutions in the vicinity of the poles

As we have seen in section 2, above, the wave-1 response has non-vanishing velocities at the poles. We now show that this is a more general property of the Matsuno-Gill model on the sphere, assuming only that Q is finite in the vicinity of the poles with no further assumptions on its spatial distribution. For the sake of simplicity, we present below an ad hoc dominant balance analysis. Alternative analysis using Fuchs' theorem to find the regular solutions in the vicinity of the (regular) singular poles (as in e.g. Bender & Orszag 1999) yields the same results but requires the assumption that $dQ/d\phi$ is also finite in the vicinity of the poles.

Consider the Matsuno-Gill model on the sphere after the Fourier decomposition, system (2.5) of the main text. Using the first row to eliminate u^m from the second and third rows yields the following second-order (inhomogeneous) system

$$\frac{d}{d\phi}\begin{bmatrix} v^m\cos\phi \\ \Phi^m \end{bmatrix} = \frac{1}{\gamma\cos\phi}\begin{bmatrix} -im\epsilon^{1/2}\sin\phi & -m^2-\gamma^2\cos^2\phi \\ -\gamma^2-\epsilon\sin^2\phi & im\epsilon^{1/2}\sin\phi \end{bmatrix}\begin{bmatrix} v^m\cos\phi \\ \Phi^m \end{bmatrix} + \begin{bmatrix} Q^m\cos\phi \\ 0 \end{bmatrix}. \tag{3.1}$$

For $m \neq 0$ and finite γ, the dominant balance in the vicinity of the poles may be obtained by: (i) Neglecting the $\gamma^2\cos^2\phi$ term, compared to the m^2 term, in the coefficient of Φ^m in the first. (2) Approximating $\sin^2\phi$ by 1 in the coefficient of $v^m\cos\phi$ in the second equation (we do not yet approximate $\sin\phi$ by 1 in order to retain the different signs at the two poles, even though its magnitude is closer to 1 than that of $\sin^2\phi$). In addition, the requirement that Q^m is finite near the poles guarantees that $Q^m\cos\phi$ vanishes as $\phi \to \pm\pi/2$, and hence the inhomogeneous term on the RHS of (3.1) can also be neglected in the dominant balance. In other words, under this assumption, the asymptotic forms of the solutions in the vicinity of the poles are determined by the unforced equations. The resulting system after neglecting these two terms is

$$\frac{d}{d\phi}\begin{bmatrix} v^m\cos\phi \\ \Phi^m \end{bmatrix} = \frac{1}{\gamma\cos\phi}\begin{bmatrix} -im\epsilon^{1/2}\sin\phi & -m^2 \\ -\gamma^2-\epsilon & im\epsilon^{1/2}\sin\phi \end{bmatrix}\begin{bmatrix} v^m\cos\phi \\ \Phi^m \end{bmatrix}. \tag{3.2}$$

To find the dominant balance we employ the following ansatz

$$v^m\cos\phi = v_p^m\cos^{\delta_1}\phi, \tag{3.3a}$$

$$\Phi^m = \Phi_p^m\cos^{\delta_2}\phi, \tag{3.3b}$$

where δ_1 and δ_2 determine the rate of decay of the solutions at the poles and v_p^m and Φ_p^m are yet unknown amplitudes (considering the meridional symmetry of the system, they may have opposite signs at the two poles). Note that, as is often the case, the dominant balance will not determine the values of v_p^m and Φ_p^m, even though they are not arbitrary in the forced problem. Substituting (3.3) into (3.2) yields the following homogeneous system for v_p^m and Φ_p^m

$$\begin{bmatrix} (\gamma\delta_1 - im\epsilon^{1/2})\cos^{\delta_1}\phi\sin\phi & -m^2\cos^{\delta_2}\phi \\ -(\gamma^2+\epsilon)\cos^{\delta_1}\phi & (\gamma\delta_2 + im\epsilon^{1/2})\cos^{\delta_2}\phi\sin\phi \end{bmatrix}\begin{bmatrix} v_p^m \\ \Phi_p^m \end{bmatrix} = \begin{bmatrix} 0 \\ 0 \end{bmatrix}. \tag{3.4}$$

The vanishing of the determinant mandates that, upon approximating $\sin^2\phi$ by 1,

$$\left[(\delta_1\delta_2 - m^2)\gamma^2 + im\epsilon^{1/2}(\delta_1-\delta_2)\gamma\right]\cos^{\delta_1+\delta_2}\phi = 0. \tag{3.5}$$

We assume that $\delta_1, \delta_2 \geqslant 0$, i.e. that the solutions are regular near the poles. Hence, the real and imaginary parts of this expression (i.e. the first and second terms in square brackets) vanish independently of each other. Thus, the dominant balance has non-trivial solutions provided

$$\delta_1 = \delta_2 := \delta = |m|. \tag{3.6}$$

The corresponding dominant balance of the zonal velocity near the poles is obtained by substituting (3.3) and (3.6) back into (2.5) of the main text. The resulting asymptotic behavior of the Matsuno-Gill model on the sphere in the vicinity of the poles, for $m \geqslant 1$ is

$$u^m \cos\phi = -i\frac{|m|}{m} v_p^m \sin\phi \cos^{|m|}\phi, \tag{3.7a}$$

$$v^m \cos\phi = v_p^m \sin\phi \cos^{|m|}\phi, \tag{3.7b}$$

$$\Phi^m = \frac{\gamma|m| - im\epsilon^{1/2}}{m^2} v_p^m \sin\phi \cos^{|m|}\phi. \tag{3.7c}$$

For $|m| > 1$, the $\cos^{|m|}\phi$ term that appears in all three equations guarantees that the zonal and meridional velocity components and the geopotential height all vanish in the vicinity of the poles. In contrast, for $|m| = 1$ the regular solutions have non-vanishing velocities in the vicinity of the poles. This apparent contradiction is alleviated by observing that the corresponding divergence vanishes identically for all $|m| \geqslant 1$, which implies that there are no net mass fluxes there. In addition, the vorticity also vanishes for all $m > 0$ (albeit not identically like the divergence). Finally, in the present work, we have only required that the solution remain regular in the vicinity of the poles, which is the most parsimonious assumption. A more physically reasonable condition may be that the winds vanish as well.

4. Asymptotic solutions

The simple solutions in section 5 of the main text, particularly the radiative relaxation (5.2), geostrophic (5.3), and non-rotating (5.4) approximations were derived by making "ad hoc" assumptions based on our observations from the representative solutions in section 4 of the main text (and sections 1 and 2 of the supplementary). As noted in the text, the geostrophic and non-rotating approximations correspond to the zero-order terms in series expansions in powers of γ and $\epsilon^{1/2}$, respectively. In this section, we show that this is indeed the case. In addition, we also consider series expansion in powers of γ^{-1} to obtain asymptotic forms of the solutions for $\gamma \gg 1$. The leading order of this approximation is slightly different from the radiative relaxation approximation obtained in the text, but compared to the numeric solutions we see no visible differences between the two. The results of this section show that the simple solutions obtained in the text are at least as good as the leading order approximations obtained here. Improvements can be made by considering the first-order corrections. Yet the improvements are mainly in terms of the accuracy and only marginally extend the region of validity. The reason is that outside those regions, the solutions become qualitatively different. Finally, a series expansion in powers of $\epsilon^{-1/2}$ does not provide a meaningful approximation of the solutions for $\epsilon^{1/2} \gg 1$. The reason is that, in this limit, the β-plane approximation becomes valid, which, as discussed in the text, is independent of $\epsilon^{1/2}$.

For the sake of readability, we re-write here the Matsuno-Gill model after introducing the Fourier decomposition, but before making any approximation:

$$-\epsilon^{1/2} v^m \sin\phi + \frac{im}{\cos\phi}\Phi^m = -\gamma u^m, \tag{4.1a}$$

$$\epsilon^{1/2} u^m \sin\phi + \frac{d\Phi^m}{d\phi} = -\gamma v^m, \tag{4.1b}$$

$$\frac{1}{\cos\phi}\left[imu^m + \frac{d}{d\phi}(v^m \cos\phi)\right] = -\gamma\Phi^m + Q^m. \tag{4.1c}$$

The series considered below may or may not converge. We only show that their leading order terms (the first non-zero terms) converge to the numeric solutions in the respective limits, and that the first corrections (the second non-zero terms) provide improvements.

4.1. *Asymptotic forms of the solutions for $\gamma \gg 1$*

To find asymptotic forms of the solutions for $\gamma \gg 1$ we attempt series solutions in powers of γ^{-1}, i.e.,

$$u^m = \sum_{j=0}^{\infty} u_j^m \gamma^{-j}, \quad v^m = \sum_{j=0}^{\infty} v_j^m \gamma^{-j}, \quad \Phi^m = \sum_{j=0}^{\infty} \Phi_j^m \gamma^{-j}. \tag{4.2a, b, c}$$

Substituting (4.2) in (4.1) and equating powers of γ^1 yields

$$u_0^m = 0, \quad v_0^m = 0, \quad \Phi_0^m = 0.$$

Equating powers of γ^0 yields

$$u_1^m = 0, \quad v_1^m = 0, \quad \Phi_1^m = Q^m.$$

Throughout this section we assume that Q^m is independent of γ and $\epsilon^{1/2}$. Hence, its only contribution in this limit is to the γ^0 terms. Equating powers of γ^{-1} yields

$$u_2^m = -\frac{im}{\cos\phi}\Phi_1^m, \quad v_2^m = -\frac{d\Phi_1^m}{d\phi}, \quad \Phi_2^m = 0.$$

Thus, the **leading order** approximation of the Matsuno-Gill model on the sphere in powers of γ^{-1} is

$$u^m = -\frac{im}{\cos\phi} Q^m \gamma^{-2}, \tag{4.3a}$$

$$v^m = -\frac{dQ^m}{d\phi} \gamma^{-2}, \tag{4.3b}$$

$$\Phi^m = Q^m \gamma^{-1}. \tag{4.3c}$$

Next, equating powers of γ^{-2} yields

$$\begin{aligned} -\epsilon^{1/2} v_2^m \sin\phi + \frac{im}{\cos\phi} \Phi_2^m &= -u_3^m, \\ \epsilon^{1/2} u_2^m \sin\phi + \frac{d\Phi_2^m}{d\phi} &= -v_3^m, \\ \frac{1}{\cos\phi}\left[im u_2^m + \frac{d}{d\phi}(v_2^m \cos\phi)\right] &= -\Phi_3^m. \end{aligned}$$

Expressions for u_3^m, v_3^m, Φ_3^m in terms of Q^m are readily obtained by substituting u_2^m, v_2^m, Φ_2^m from above. The resulting **first correction** is

$$u^m = -\frac{im}{\cos\phi} Q^m \gamma^{-2} - \epsilon^{1/2} \sin\phi \frac{dQ^m}{d\phi} \gamma^{-3}, \tag{4.4a}$$

$$v^m = -\frac{dQ^m}{d\phi} \gamma^{-2} + im\epsilon^{1/2} \tan\phi Q^m \gamma^{-3}, \tag{4.4b}$$

$$\Phi^m = Q^m \gamma^{-1} + \left(\frac{d^2 Q^m}{d\phi^2} - \tan\phi \frac{dQ^m}{d\phi} - \frac{m^2}{\cos^2\phi} Q^m \right) \gamma^{-3}. \tag{4.4c}$$

Comparing (4.4) to (5.21) of the main text we see that the wind components of the radiative relaxation approximation are consistent with the first correction obtained above when the $\epsilon \sin^2\phi$ term in the denominator can be neglected compared to γ^2. In terms of the geopotential, the radiative relaxation approximation in (5.19) of the main text corresponds only to the leading order obtained above.

Figures 7 and 8 show the relative difference between the numeric solutions and the leading order (4.3) and first correction (4.4) as a function of γ and $\epsilon^{1/2}$. Comparing figure 7 to figure 8 of the main text, we see no difference between the leading order in powers of γ^{-1} and the radiative relaxation approximation. The first correction in figure 8 improves the accuracy (smaller log differences, darker shades), but barely increases the region of validity of this approximation.

4.2. *Asymptotic forms of the solutions for* $\gamma \ll 1$

To find asymptotic forms of the solutions for $\gamma \ll 1$ we attempt series solutions in powers of γ, i.e.,

$$u^m = \sum_{j=0}^{\infty} u_j^m \gamma^j, \quad v^m = \sum_{j=0}^{\infty} v_j^m \gamma^j, \quad \Phi^m = \sum_{j=0}^{\infty} \Phi_j^m \gamma^j. \tag{4.5a, b, c}$$

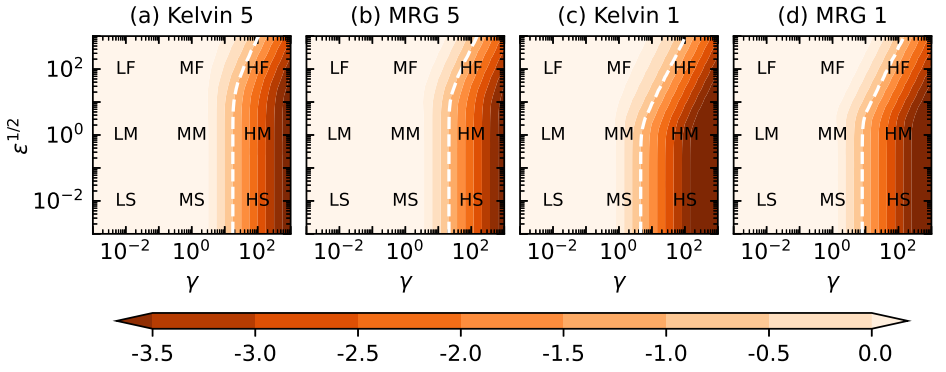


FIGURE 7. **Leading order in powers of γ^{-1}.** Same as figure 8 of the main text, but for the relative difference between (4.3) and the numeric solutions.

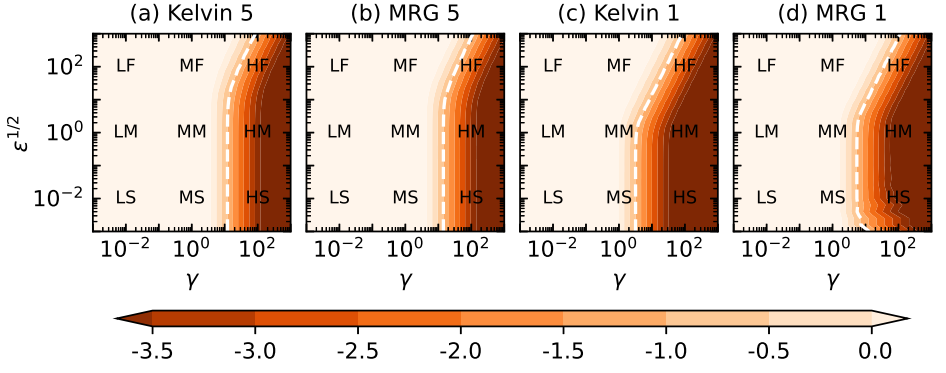


FIGURE 8. **First correction in powers of γ^{-1}.** Same as figure 8 of the main text, but for the relative difference between (4.4), and the numeric solutions.

Substituting (4.5) in (4.1) and equating powers of γ^0 yields

$$-\epsilon^{1/2} v_0^m \sin\phi + \frac{im}{\cos\phi}\Phi_0^m = 0,$$
$$\epsilon^{1/2} u_0^m \sin\phi + \frac{d\Phi_0^m}{d\phi} = 0,$$
$$\frac{1}{\cos\phi}\left[imu_0^m + \frac{d}{d\phi}(v_0^m \cos\phi)\right] = Q^m.$$

Again, we assume that Q^m is independent of γ and ϵ and, hence, its only contribution in this limit is to the γ^0 terms. The above system is exactly the geostrophic approximation (5.22) of the main text. As detailed in the main text, using the first two equations to substitute for u_0^m and v_0^m in the third equation yields an algebraic expression for Φ_0^m in terms of Q^m (the $d\Phi_0^m/d\phi$ derivative terms cancel out), which can then be back substituted into the first two equations to obtain expressions for u_0^m and v_0^m in terms of Q^m. The resulting **leading order** approximation of the Matsuno-Gill model on the

sphere in powers of γ is

$$\Phi^m = \epsilon^{1/2}\frac{i}{m}\sin^2\phi Q^m, \tag{4.6a}$$

$$u^m = -2\frac{i}{m}\cos\phi Q^m - \frac{i}{m}\sin\phi\frac{dQ^m}{d\phi}, \tag{4.6b}$$

$$v^m = -\tan\phi Q^m. \tag{4.6c}$$

Next, equating powers of γ^1 yields

$$-\epsilon^{1/2}v_1^m\sin\phi + \frac{im}{\cos\phi}\Phi_1^m = -u_0^m,$$

$$\epsilon^{1/2}u_1^m\sin\phi + \frac{d\Phi_1^m}{d\phi} = -v_0^m,$$

$$\frac{1}{\cos\phi}\left[imu_1^m + \frac{d}{d\phi}(v_1^m\cos\phi)\right] = -\Phi_0^m.$$

The procedure for solving this system is the same as above. Upon using the first two equations to substitute for u_1^m and v_1^m in the third equation, the $d\Phi_1^m/d\phi$ derivative terms cancel out, leaving an algebraic expression for Φ_1^m in terms of Q^m. The solution is

$$\begin{aligned} m^2\Phi_1^m &= -\sin^2\phi\frac{d^2Q^m}{d\phi^2} \\ &\quad + \left[-3\cos\phi + \frac{1}{\cos\phi}\right]\sin\phi\frac{dQ^m}{d\phi} \\ &\quad + \left[2 + 2\sin^2\phi + \tan^2\phi + \epsilon\sin^4\phi\right]Q^m, \end{aligned} \tag{4.7a}$$

$$\begin{aligned} \epsilon^{1/2}m^2\sin\phi u_1^m &= \sin^2\phi\frac{d^3Q^m}{d\phi^3} \\ &\quad - \left[-5\cos\phi + \frac{1}{\cos\phi}\right]\sin\phi\frac{d^2Q^m}{d\phi^2} \\ &\quad - \left[8\sin^2\phi + (m^2+1)\tan^2\phi + \epsilon\sin^4\phi\right]\frac{dQ^m}{d\phi} \\ &\quad - \left[4\sin\phi\cos\phi + m^2\left(\frac{2}{\cos^2\phi} - 1\right)\tan\phi + 4\epsilon\sin^3\phi\cos\phi\right]Q^m, \end{aligned} \tag{4.7b}$$

$$\begin{aligned} \epsilon^{1/2}m^2\sin\phi v_1^m &= -\sin^2\phi\frac{im}{\cos\phi}\frac{d^2Q^m}{d\phi^2} \\ &\quad + \frac{im}{\cos\phi}\left[-4\cos\phi + \frac{1}{\cos\phi}\right]\sin\phi\frac{dQ^m}{d\phi} \\ &\quad + \frac{im}{\cos\phi}\left[4\sin^2\phi + m^2\tan^2\phi + \epsilon\sin^4\phi\right]Q^m. \end{aligned} \tag{4.7c}$$

Figures 9 and 10 show the relative difference between the numeric solutions and the leading order and first correction as a function of γ and $\epsilon^{1/2}$. The leading order is simply given by (4.6). The first correction is given by (4.6) + (4.7) γ. Again, the leading order is exactly the same as the geostrophic approximation in the main text. Accordingly figure 9 is the same as figure 10 of the main text. Comparing figures 9 and 10, the first correction improves the accuracy (smaller log differences, darker shades), and slightly increases the region of validity of this approximation (the white dashed line moves to higher values of γ). The improvement in the region of validity is limited by the fact that, as observed in

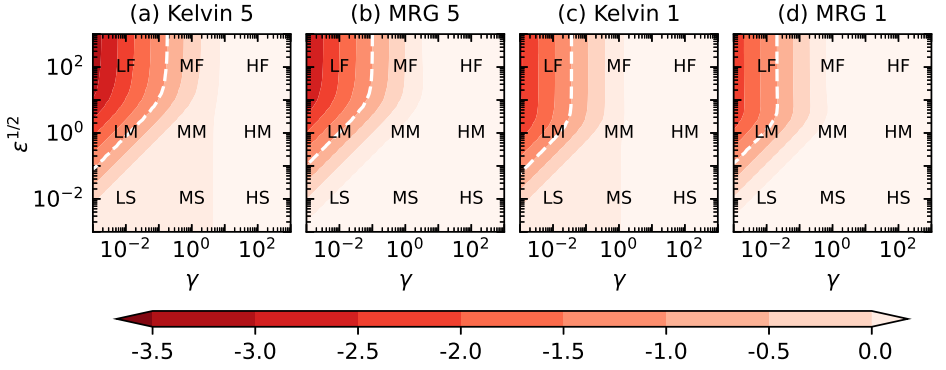


FIGURE 9. **Leading order in powers of γ.** Same as figure 10 of the main text, but for the relative difference between (4.6) and the numeric solutions.

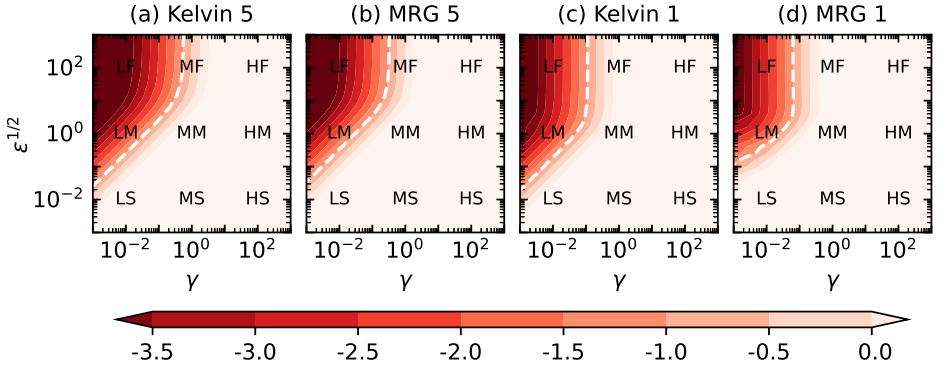


FIGURE 10. **First correction in powers of γ.** Same as figure 10 of the main text, but for the relative difference between the first correction, calculated as (4.6) + (4.7) γ, and the numeric solutions.

the representative examples, the solutions become qualitatively a-geostrophic outside this region. The approximation in powers of γ becomes inaccurate at slow rotation, which is a reflection of the fact that the Matsuno-Gill model is underdetermined when $\gamma = \epsilon^{1/2} = 0$ (see section 5.5 of the main text).

4.3. *Asymptotic forms of the solutions for $\epsilon^{1/2} \ll 1$*

To find asymptotic forms of the solutions for $\epsilon^{1/2} \ll 1$ we attempt series solutions in powers of $\epsilon^{1/2}$, i.e.,

$$u^m = \sum_{j=0}^{\infty} u_j^m \epsilon^{j/2}, \quad v^m = \sum_{j=0}^{\infty} v_j^m \epsilon^{j/2}, \quad \Phi^m = \sum_{j=0}^{\infty} \Phi_j^m \epsilon^{j/2}. \tag{4.8a, b, c}$$

Substituting (4.8) in (4.1) and equating powers of $(\epsilon^{1/2})^0$ yields

$$\begin{aligned}\frac{im}{\cos\phi}\Phi_0^m &= -\gamma u_0^m,\\ \frac{d\Phi_0^m}{d\phi} &= -\gamma v_0^m,\\ \frac{1}{\cos\phi}\left[imu_0^m + \frac{d}{d\phi}(v_0^m\cos\phi)\right] &= -\gamma\Phi_0^m + Q^m.\end{aligned}$$

This is exactly the non-rotating approximation (5.26) of the main text. As detailed in the main text, this system can be reduced to a Helmholtz (like) equation for Φ_0^m, which can be solved by expanding the forcing in Associated Legendre Polynomials (ALPs). Fortunately, for $\epsilon^{1/2} \ll 1$ the geopotential height field associated with the Kelvin and MRG waves can be accurately approximated by a single ALP, i.e.,

$$Q^m(\phi) = Q_f^m P_l^m(\sin\phi), \tag{4.9}$$

where Q_f^m is a constant amplitude, and $l = m$ or $l = m+1$ for Kelvin or MRG waves, respectively. The resulting **leading order** approximation of the Matsuno-Gill model on the sphere in powers of $\epsilon^{1/2}$ is

$$\Phi^m = \frac{\gamma}{\gamma^2 + l(l+1)} Q_f^m P_l^m(\sin\phi), \tag{4.10a}$$

$$u^m = -\frac{im}{\gamma^2 + l(l+1)} \frac{Q_f^m}{\cos\phi} P_l^m(\sin\phi), \tag{4.10b}$$

$$v^m = -\frac{1}{\gamma^2 + l(l+1)} Q_f^m \frac{dP_l^m(\sin\phi)}{d\phi}. \tag{4.10c}$$

Next, equating powers of $(\epsilon^{1/2})^1$ yields

$$\begin{aligned}-v_0^m\sin\phi + \frac{im}{\cos\phi}\Phi_1^m &= -\gamma u_1^m,\\ u_0^m\sin\phi + \frac{d\Phi_1^m}{d\phi} &= -\gamma v_1^m,\\ \frac{1}{\cos\phi}\left[imu_1^m + \frac{d}{d\phi}(v_1^m\cos\phi)\right] &= -\gamma\Phi_1^m.\end{aligned}$$

The procedure for solving this system is the same as above. First it is transformed into the following Helmholtz (like) equation for Φ_1^m

$$\Delta^m\Phi_1^m = \gamma^2\Phi_1^m + im\gamma^{-1}\Phi_0^m,$$

where the m-restricted Laplacian (Δ^m) is defined in (5.28) of the main text. Now, the role of the forcing is played by Φ_0^m, which is proportional to a single ALP. Hence, this equation can be readily solved as in the main text. The solution, after back substituting Φ_1^m to obtain u_1^m and v_1^m, is

$$\Phi_1^m = -\frac{im}{(\gamma^2 + l(l+1))^2} Q_f^m P_l^m(\sin\phi), \tag{4.11a}$$

$$\gamma u_1^m = -\frac{m^2}{(\gamma^2 + l(l+1))^2} \frac{Q_f^m}{\cos\phi} P_l^m(\sin\phi) - \frac{\sin\phi}{\gamma^2 + l(l+1)} Q_f^m \frac{dP_l^m(\sin\phi)}{d\phi}, \tag{4.11b}$$

$$\gamma v_1^m = \frac{im}{(\gamma^2 + l(l+1))^2} Q_f^m \frac{dP_l^m(\sin\phi)}{d\phi} + \frac{im\sin\phi}{\gamma^2 + l(l+1)} \frac{Q_f^m}{\cos\phi} P_l^m(\sin\phi). \tag{4.11c}$$

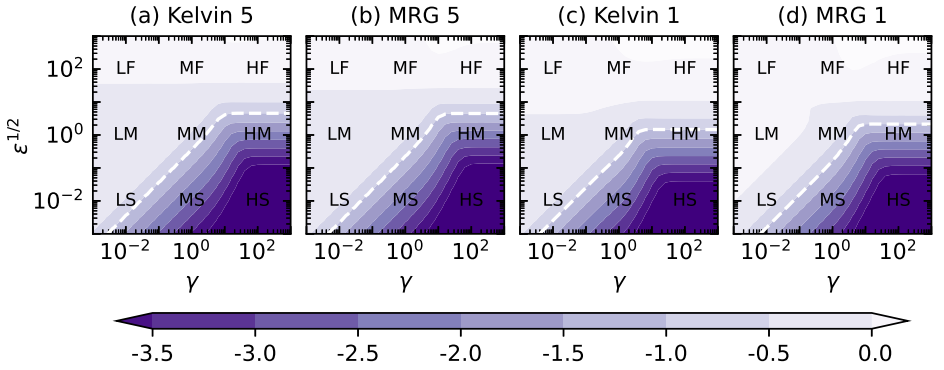


FIGURE 11. **Leading order in powers of $\epsilon^{1/2}$.** Same as figure 12 of the main text, but for the relative difference between (4.10) and the numeric solutions.

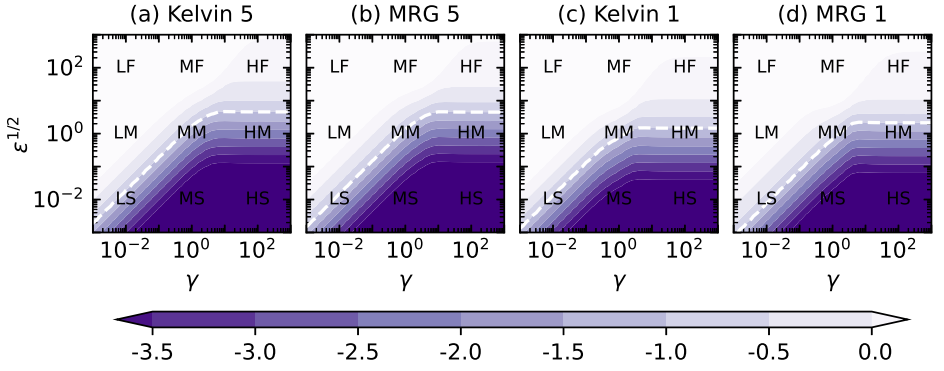


FIGURE 12. **First correction in powers of $\epsilon^{1/2}$.** Same as figure 12 of the main text, but for the relative difference between the first correction, calculated as (4.10) + (4.11) $\epsilon^{1/2}$, and the numeric solutions.

Figures 11 and 12 show the relative difference between the numeric solutions and the leading order and first correction as a function of γ and $\epsilon^{1/2}$. The leading order is simply given by (4.10). The first correction is given by (4.10) + (4.11) $\epsilon^{1/2}$. Again, the leading order is exactly the same as the non-rotating approximation in the main text. Accordingly figure 11 is the same as figure 12 of the main text. Comparing figures 11 and 12 (here), the first correction improves the accuracy (smaller log differences, darker shades), and slightly increases the region of validity of this approximation (the white dashed line moves to smaller values of γ). The improvement in the region of validity is limited by the fact that the solutions become qualitatively different from non-rotating outside this region. The approximation in powers of $\epsilon^{1/2}$ becomes inaccurate at light damping, which is a reflection of the fact that the Matsuno-Gill model is underdetermined when $\gamma = \epsilon^{1/2} = 0$ (see section 5.5 of the main text).

5. Wave spectrum for small wavenumber forcing

Due to the fact that the applied forcing consists only of the geopotential height field of the Kelvin wave (for symmetric forcing), and the fact that the polarization relations between u, v, Φ involve the wavenumber, the excited waves depend on the forcing wavenumber as well. We now examine the effects of the forcing wavenumber on the response spectrum. We focus only on the fast rotation cases, where the equatorial β-plane approximation is accurate and we can examine fractional wavenumbers below $m = 1$. The resulting projections on the free EIG2, EIG1, EIG0, Kelvin, Rossby2, Rossby1, MRG, WIG1, and WIG2 wave modes are given in Table 1, for a Kelvin wave (a) $m = 2$, (b) $m = 1$, (c) $m = 0.5$, and (d) $m = 0.1$ forcing.

The key observation from this table is the relative contributions of the Kelvin and Rossby1 waves in the moderate damping and fast rotation (MF) case, corresponding to the parameters used by Matsuno and Gill. As the forcing wavenumber decreases the Kelvin wave contribution increase and the Rossby1 wave contribution decreases. For a forcing wavenumber $m = 1$, the Rossby1 wave still accounts for about two-thirds of the response. As the forcing wavenumber decreases below 1, the Kelvin wave becomes the dominant part of the response eventually. This is consistent with the distribution of the Kelvin and Rossby1 waves in Gill's study, where the localized heat source projects on small wavenumbers.

Finally, the wave spectrum in the heavy damping and fast rotation (HF) case appears to be independent of the forcing wavenumber between $m = 2$ and $m = 0.1$ considered in the table. However, it is noticeably different from the forcing wavenumber $m = 5$ considered in the main text.

	EIG2	EIG1	EIG0	Kelvin	Rossby2	Rossby1	MRG	WIG1	WIG2	Sum
(a) Kelvin $m = 2$ response										
LF	-	45%	-	-	-	8%	-	47%	-	100%
MF	-	-	-	12%	-	88%	-	-	-	100%
HF	-	4%	-	51%	-	32%	-	12%	-	100%
(b) Kelvin $m = 1$ response										
LF	-	29%	-	1%	-	40%	-	30%	-	100%
MF	-	-	-	32%	-	68%	-	-	-	100%
HF	-	4%	-	51%	-	33%	-	12%	-	100%
(c) Kelvin $m = 0.5$ response										
LF	-	4%	-	2%	-	90%	-	4%	-	100%
MF	-	-	-	50%	-	50%	-	-	-	100%
HF	-	5%	-	51%	-	33%	-	11%	-	100%
(d) Kelvin $m = 0.1$ response										
LF	-	-	-	2%	-	98%	-	-	-	100%
MF	-	-	-	60%	-	40%	-	-	-	100%
HF	-	5%	-	51%	-	34%	-	11%	-	100%

TABLE 1. Projections of the Matsuno-Gill model solutions on the free RSWEs wave modes in response to a Kelvin wave (a) $m = 2$, (b) $m = 1$, (c) $m = 0.5$, and (d) $m = 0.1$ forcing. Reported values correspond to the percent fraction (accurate to 1%) of the total power projected on the (columns from left to right): EIG2, EIG1, EIG0, Kelvin, Rossby2, Rossby1, MRG, WIG1, and WIG2 wave modes. The classification of the modes follows the classification used in Matsuno (1966). The combined contribution of the eight modes is given in the last column from the left. The different rows correspond to the 9 samples of the $(\gamma, \epsilon^{1/2})$ plane given in Table 1 of the main text. To improve the readability, 0% projections, to the retained accuracy, are replaced by dashes.

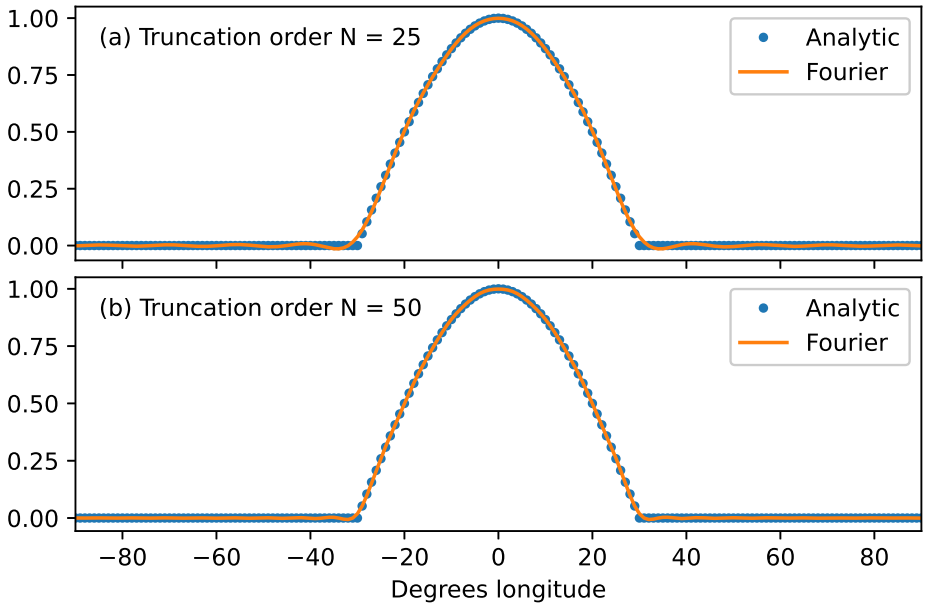


FIGURE 13. The longitudinal part of the localized forcing in (8.1) of the main text (blue dots), compared to the Fourier decomposition in (8.2) of the main text (orange line), for truncation orders (a) 25 and (b) 50. For clarity, only half of the zonal domain $-\pi/2 \leqslant \lambda \leqslant \pi/2$ is shown.

6. Sensitivity of the Fourier decomposition to the truncation order

In section 8 of the main text we study the response to a localized forcing akin to that used by Gill (1980) by solving for the latitude-dependent boundary value problem remaining after a Fourier decomposition in the zonal direction. The convergence of the analytically derived Fourier series in (8.2) of the main text to the forcing in (8.1) of the main text is shown in figure 13 for truncation orders (a) 25 and (b) 50. With a truncation order 25 there are still noticeable differences, whereas for a truncation order 50 the two are nearly indistinguishable. The results presented in the main text were obtained using a truncation order 50. There appear to be vanishing oscillations near the discontinuity in the derivative of the forcing at $\lambda = \pm\pi/6$. There is no Gibbs phenomenon of non-vanishing oscillations characteristic of points of discontinuity in the function itself. Yet, the implications of the discontinuity in the derivative, and the oscillations near the points of discontinuity, should be re-examined in the presence of non-linearities.



FIGURE 14.
Title: Element of coat of arms (Fleur-de-lis).
Artist: SODACAN (https://commons.wikimedia.org/wiki/User:Sodacan)
Source: https://commons.wikimedia.org/wiki/File:Fleur_de_lys_(or).svg
Copyright information: Creative Commons Attribution 1.0 Generic (CC BY 1.0)
license: https://creativecommons.org/licenses/by/1.0/legalcode

7. Flora

In an attempt to establish a mnemonic device for the prevalent solution pattern of the the Matsuno-Gill model (figure 1b of the main text) we have introduced the neologism "La Fleur-de-lis". This was inspired by Matsuno's description of the pressure cells as petals of a flower, and the omnipresent Fleur-de-lis emblem. Yet, the reader may not know this emblem, and it has variations. Thus we provide an example here. We hope that the reader does not take our analogy too literally. There is also debate on which flower is actually depicted.

REFERENCES

Bender, C. M. & Orszag, S. A. 1999 *Advanced mathematical methods for scientists and engineers I: Asymptotic methods and perturbation theory*. New York, NY: Springer Science & Business Media.

Gill, A. E. 1980 Some simple solutions for heat-induced tropical circulation. *Quarterly Journal of the Royal Meteorological Society* **106** (449), 447–462.

Matsuno, T. 1966 Quasi-geostrophic motions in the equatorial area. *J. Meteor. Soc. Japan* **44** (1), 25–43.